nature synthesis

Article

https://doi.org/10.1038/s44160-025-00769-9

Industrial-level CO_2 to formate conversion on Turing-structured electrocatalysts

Received: 20 October 2024

Accepted: 14 February 2025

Published online: 20 March 2025

Check for updates

Na Ye[1,3], Kai Wang[1,3], Yingjun Tan[1,3], Zhengyi Qian[1], Hongyu Guo[1], Changshuai Shang[1], Zheng Lin[1], Qizheng Huang[1], Youxing Liu[1], Lu Li[1], Yu Gu[1], Ying Han[1], Chenhui Zhou[1], Mingchuan Luo[1] & Shaojun Guo[1,2]

Industrializing the electrosynthesis of formate from CO_2 reduction in membrane electrode assembly (MEA) electrolysers necessitates tuning both electrocatalysts and the interfacial water microenvironment. Here we cast a series of Turing-structured topology electrocatalysts, which can control the reorientation of interfacial water through the tuning of surface oxophilicity, for industrial-level conversion of CO_2 to formate. Experimental and theoretical results verify the precisely modulated reorientation of interfacial water, with the ratios of four-coordinated to two-coordinated hydrogen-bonded interfacial water ranging from 0.26 to 3.10 over Turing-structured topology catalysts. We further demonstrate the efficiency of these strategies in sustaining high-rate formate electrosynthesis across a wide range of industrial-level current densities (300–1,000 mA cm^{-2}) and formulate a volcano relationship to describe the relation. The optimal Turing $Sb_{0.1}Sn_{0.9}O_2$ catalyst achieves a formate Faradaic efficiency of 92.0% at 1,000 mA cm^{-2} and exhibits a stability of 200 h at 500 mA cm^{-2} in a membrane electrode assembly electrolyser. Our findings highlight the prospect of topology-mediated tunings of the interfacial water microenvironment for electrifying the conversion of CO_2 to formate, with promising implications for the electrosynthesis of other valuable chemicals.

The electrochemical reduction of CO_2 (CO_2RR) offers a sustainable route for converting renewable electricity and carbon emissions into value-added liquid feedstocks such as formates[1–5]. Among various catalysts capable of producing formates, tin-based catalysts stand out due to their abundance, environmental friendliness and appropriate adsorption of intermediates[6,7]. However, despite extensive efforts at catalyst optimization, existing catalysts fail to sustain satisfactory selectivity and stability at current densities of >200 mA cm^{-2} (refs. 8–11), which severely hinders their further application in practical membrane electrode assembly (MEA) electrolysers.

Studies have shown that the modulation of the local microenvironment serves as another viable approach to tune CO_2RR electrocatalysis[12–15], because the hydrogenation of CO_2RR involves hydrogen transfer from the reaction microenvironment[3,16–18]. Although hydrogen transfer is necessary for the protonation of CO_2, excessive hydrogen transfer can promote the competitive hydrogen evolution reaction (HER), which seriously hinders the CO_2RR at high industrial-level current densities[19–22]. It is therefore crucial to regulate the local microenvironment for optimal hydrogen transfer rates to realize the electrosynthesis of formate at industrial scales. Under CO_2RR-relevant alkaline microenvironments, H_2O-dominated hydrogen-bond networks govern the hydrogen transfer rate in several electrochemical reactions, such as the HER/hydrogen oxidation reaction and the oxygen reduction reaction[19–23]. This strategy has been extended to the CO_2RR generally by tuning the bulk electrolyte properties, such as cation addition or organic solvent incorporation[12,13,16] to optimize the hydrogen-bond networks. However, the limited solubility and stability of these additives severely impede the practical

[1]School of Materials Science and Engineering, Peking University, Beijing, People's Republic of China. [2]Laoshan Laboratory, Qingdao, People's Republic of China. [3]These authors contributed equally: Na Ye, Kai Wang, Yingjun Tan. e-mail: guosj@pku.edu.cn

application of this strategy. We reason that the local microenvironment is a function of both bulk electrolyte and the electrode surface because the thermodynamics of the latter two govern the ultimate status of the former[22]. Following this reasoning, the local microenvironment can be also manipulated by engineering the surface properties of electrocatalysts, and this approach should be more robust and practical than bulk electrolyte tunings for the CO_2RR in MEA electrolysers. Specifically, the surface topology of an electrode may serve as a straightforward means to tune the interfacial hydrogen-bond networks, which transcends traditional approaches to enhancing CO_2RR.

Here we cast a series of Turing-structured topology electrocatalysts, and manipulated the interfacial hydrogen-bond networks by tuning their surface oxophilicity to achieve industrial-level CO_2-to-formate conversion. Through physical characterizations, in situ spectroscopies and theoretical analysis, we established the mechanistic relation between the oxophilicity of the Turing-type catalysts and the formate electrosynthesis efficiency on the basis of the orientations of four-coordinated/two-coordinated, hydrogen-bonded interfacial water (4-HB/2-HB interfacial water) within hydrogen-bond networks. Specifically, we find that a small ratio of 4-HB/2-HB interfacial water (weak oxophilicity) hinders the protonation of CO_2 to generate *OCHO intermediates, and a large ratio of 4-HB/2-HB interfacial water (strong oxophilicity) promotes a competitive HER by accelerating the hydrogen transfer. We further demonstrate the high efficiency of this strategy in sustaining high-rate formate electrosynthesis. The optimal Turing $Sb_{0.1}Sn_{0.9}O_2$ delivered a formate Faradaic efficiency of 92.0% at 1,000 mA cm^{-2} in a flow cell system and stability over 200 h at 500 mA cm^{-2} in a MEA electrolyser. Our findings open up avenues for tuning the interfacial water microenvironment mediated by the topology of electrocatalyst, which holds practical implications.

Results and discussion

Synthesis and characterization of Turing $Sb_{0.1}Sn_{0.9}O_2$

Reduced oxidized graphene (rGO), as a sacrificial template, has the structural advantages of a well-defined layer structure and oxygen-containing functional groups on the surface, making it possible to simultaneously synthesize ultrafine nanostructured metal oxides. Ultrathin two-dimensional (2D) Turing-type $Sb_{0.1}Sn_{0.9}O_2$ nanosheets were synthesized by using rGO as a template, followed by heat treatment to remove the rGO template. As a comparison, Turing-type SnO_2 nanosheets were prepared identically, except for the absence of the antimony precursor (Supplementary Fig. 1). Because this method depends on the balance between the growth and nucleation of metal oxides, it can be used to construct various Turing-type metal oxide nanosheets (Supplementary Figs. 2–5). To gain deeper insight into the advantages of 2D Turing-type $Sb_{0.1}Sn_{0.9}O_2$ nanosheets, a commercial $Sb_{0.1}Sn_{0.9}O_2$ nanoparticle catalyst, 2D non-Turing $Sb_{0.1}Sn_{0.9}O_2$ nanosheets and 2D SnO_2 nanosheets were also selected as control catalysts (Supplementary Figs. 6–11). Inductively coupled plasma spectroscopy indicates that the as-prepared Turing $Sb_{0.1}Sn_{0.9}O_2$ catalyst contains 10.5 wt% tin and 89.5 wt% antimony. The X-ray diffraction (XRD) pattern (Supplementary Fig. 12) of Turing $Sb_{0.1}Sn_{0.9}O_2$ matches well with that of SnO_2, demonstrating that antimony atoms were successfully incorporated into SnO_2 to form solid solutions.

Transmission electron microscopy (TEM) images (Fig. 1a,b) of the Turing $Sb_{0.1}Sn_{0.9}O_2$ catalyst show the morphology of holey 2D nanosheets with a specific surface area of 66.28 m^2 g^{-1} (Supplementary Fig. 13). As shown by high-resolution transmission electron microscopy (HRTEM) (Fig. 1c), the Turing $Sb_{0.1}Sn_{0.9}O_2$ catalyst is composed of multiple chains around 5 nm in diameter with various orientations, which are interconnected to create a continuous network with plenty of grain boundaries. The branched grains topologically look like Turing patterns, as occur in the biosphere, such as human fingerprints and certain mollusk shells[24–30]. Therefore, the $Sb_{0.1}Sn_{0.9}O_2$ nanosheets in the work are also represented as Turing-type $Sb_{0.1}Sn_{0.9}O_2$ due to their Turing-type topological morphology.

The aberration-corrected high-angle annular dark-field scanning transmission electron microscopy (HAADF-STEM) image in Fig. 1d clearly shows a number of grain boundaries with various crystallographic planes and orientations in Turing $Sb_{0.1}Sn_{0.9}O_2$, in agreement with the results observed in the fast Fourier transform images (Fig. 1d). The grains in Turing $Sb_{0.1}Sn_{0.9}O_2$ match well with the twinning grain boundaries with one or more atomic-layer mismatches. These crystalline defects or lattice distortions can induce strain, as further confirmed by the non-uniform colour distributions at grain boundaries in the geometric phase analysis mapping images (Fig. 1e–g). This also validates the crystallographic characteristic of Turing structures, namely, that they can adapt to mismatched orientations of nanocrystals constrained by neighbouring nanograins[24]. In addition, the corresponding energy-dispersive X-ray spectroscopy (EDS) elemental mapping (Fig. 1h) and line scanning profiles (Supplementary Fig. 14) verify the uniform distribution of tin and antimony in Turing $Sb_{0.1}Sn_{0.9}O_2$.

Based on the above crystallographic characterization, a schematic diagram of Turing $Sb_{0.1}Sn_{0.9}O_2$ nanograins is depicted in Fig. 1i. The thickness of Turing $Sb_{0.1}Sn_{0.9}O_2$ is determined to be ~1.65 nm by atomic force microscopy (Fig. 2a), implying its ultrathin nature. Turing $Sb_{0.1}Sn_{0.9}O_2$ shows a stronger electron paramagnetic resonance intensity relative to other references (Fig. 2b), revealing its defects, which could improve the electronic conductivity[28]. In consequence, the ultrathin 2D Turing $Sb_{0.1}Sn_{0.9}O_2$ was fabricated successfully with multiple twin boundaries and defects, which are intrinsic characteristics of the Turing configuration.

To reveal the surface chemical states and local coordination information of Turing $Sb_{0.1}Sn_{0.9}O_2$, X-ray photoelectron spectroscopy (XPS), X-ray absorption near-edge structure (XANES) and extended X-ray absorption fine structure (EXAFS) experiments were carried out. The high-resolution XPS (Fig. 2c) and valence band (Fig. 2d) results illustrate that both the Sn 3*d* peak and the valence band of Turing $Sb_{0.1}Sn_{0.9}O_2$ present downshifted peaks in comparison with those of Turing SnO_2, implying that antimony incorporation contributes to the electronic interaction and a downshifted p-band centre. The white line peak and the absorption edge of Turing $Sb_{0.1}Sn_{0.9}O_2$ in XANES spectra (Fig. 2e) are slightly higher than those of Turing SnO_2, revealing that the valence state of Turing $Sb_{0.1}Sn_{0.9}O_2$ is slightly higher than that of Turing SnO_2, in agreement with the Sn 3*d* XPS results.

As shown in the Fourier-transformed EXAFS spectra and corresponding fitting curve results (Fig. 2f and Supplementary Table 1), SnO_2 presents two dominant peaks at around 2.05 Å and 3.70 Å, assigned to the Sn–O and Sn–Sn (or Sn–O–Sn) distances, respectively. In contrast, Turing SnO_2 shows a longer Sn–O–Sn distance (3.73 Å) than that of SnO_2, suggesting that Turing structures lead to a long atomic distance, caused by the lattice strain[24]. Additionally, the Sn–O–Sn distance of Turing $Sb_{0.1}Sn_{0.9}O_2$ is 3.72 Å, slightly shorter than that of Turing SnO_2, consistent with the downshifted p-band centre after antimony doping in the XPS valence band analysis.

Both the intensity of Sn–O–Sn peaks (Fig. 2f) and corresponding fitting coordination number (Supplementary Table 1) follow the same sequences: SnO_2 > Turing SnO_2 > Turing $Sb_{0.1}Sn_{0.9}O_2$. The low coordination numbers in ultrathin Turing structures result from the formation of high-density defects and twin boundaries, which could have a positive effect on the oxophilicity properties and on the induced catalytic performances[24,25]. Additionally, both Turing $Sb_{0.1}Sn_{0.9}O_2$ and Turing SnO_2 present similar wavelet transforms (Fig. 2g–j), further suggesting the successful formation of solid solutions, consistent with XRD results. In short, the above characterizations demonstrate the features of ultrathin 2D Turing-type $Sb_{0.1}Sn_{0.9}O_2$ nanosheets with abundant twin boundaries and defects, which can induce uncoordinated coordination number and tunable oxophilicity.

https://doi.org/10.1038/s44160-025-00769-9

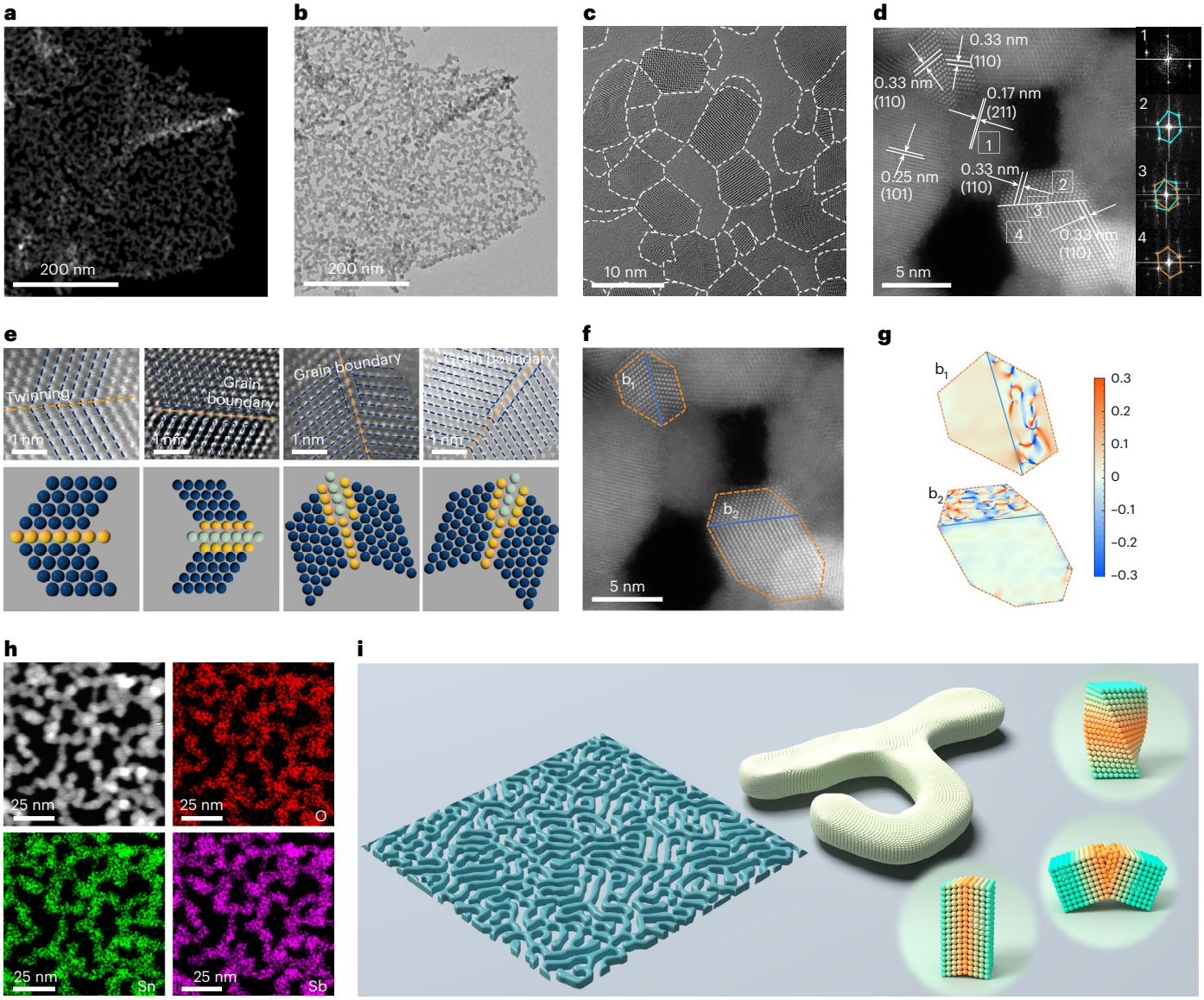

Fig. 1 | Microstructures of the Turing $Sb_{0.1}Sn_{0.9}O_2$ catalyst. a, Dark-field TEM image. **b**, TEM image. **c**, HRTEM image, with white dashed lines highlighting abundant grain boundaries. **d**, HAADF-STEM image. Inset: fast Fourier transform images of the marked areas. The blue hexagons (middle right) and orange hexagons (bottom right) mean different types of crystalline planes. **e**, HAADF-STEM images showing the presence of twinning (top left) and different types of grain boundaries (top centre and top right) of nanoparticles. The dashed lines (top) and blue spheres (bottom) denote the atomic arrangement directions and the metal atoms of the Turing $Sb_{0.1}Sn_{0.9}O_2$ catalyst, respectively. The orange and green spheres (bottom) highlight metal atoms different types of grain boundary. **f**, HAADF-STEM image, with b_1 and b_2 corresponding to different field of grain boundary. The orange lines (top left and bottom right) denote the boundaries of b_1 and b_2. The blue lines (top left and bottom right) denote grain boundaries. **g**, Geometric phase analysis mapping images corresponding to the field of b_1 and b_2 in **f**. The colour bar means the strength of the in-plane strain. **h**, EDS elemental mapping images. **i**, Schematic diagram of the Turing $Sb_{0.1}Sn_{0.9}O_2$ catalyst (left) and corresponding crystallographic characterization (right).

Electrochemical CO_2RR performance in flow cells and MEAs

To validate the prospects of Turing $Sb_{0.1}Sn_{0.9}O_2$ at ampere-level current densities, the electrochemical CO_2RR performance of Turing $Sb_{0.1}Sn_{0.9}O_2$ was evaluated using flow cells with 0.5 M $KHCO_3$ (Supplementary Fig. 15). Linear sweep voltammetry (LSV) curves under a CO_2 atmosphere (Fig. 3a,b and Supplementary Figs. 16 and 17) reveal that Turing $Sb_{0.1}Sn_{0.9}O_2$ achieves a current density of up to 1,000 mA cm^{-2} at only −1.6 V, higher than the densities of Turing SnO_2 (600 mA cm^{-2}), commercial $Sb_{0.1}Sn_{0.9}O_2$ (200 mA cm^{-2}) and commercial SnO_2 (200 mA cm^{-2}), highlighting its superior CO_2RR activity and kinetics at ampere-level current densities. Turing $Sb_{0.1}Sn_{0.9}O_2$ also exhibits much higher Faradaic efficiency (FE) for formates (up to 95.7%) than other control catalysts at various current densities, especially for high current densities (Fig. 3a,b and Supplementary Fig. 18). Specifically, Turing $Sb_{0.1}Sn_{0.9}O_2$ presents a $FE_{formate}$ of 91.8% at 1,000 mA cm^{-2}, higher than those of Turing SnO_2 (65.1%), commercial $Sb_{0.1}Sn_{0.9}O_2$ (~0) and commercial SnO_2 (~0) at 1,000 mA cm^{-2}. In particular, it is also found that the catalytic activities and $FE_{formate}$ of Turing configurations are superior to those of non-Turing-type catalysts, illustrating that Turing configurations are more favourable for CO_2 electroreduction to formates, especially at large current densities. The partial current densities of formate ($J_{formate}$) (Fig. 3c) at various potentials on Turing $Sb_{0.1}Sn_{0.9}O_2$ and other reference catalysts exhibit a similar activity trend, further endorsing the superiority of Turing $Sb_{0.1}Sn_{0.9}O_2$ in the electrochemical CO_2-to-formate conversion at ampere-level current densities. The properties of the electrode–electrolyte interfaces were also studied. Impressively, Turing $Sb_{0.1}Sn_{0.9}O_2$ presents a very large electrochemically active surface area (Supplementary Fig. 19) of 261.8 cm^2 cm^{-2} compared

https://doi.org/10.1038/s44160-025-00769-9

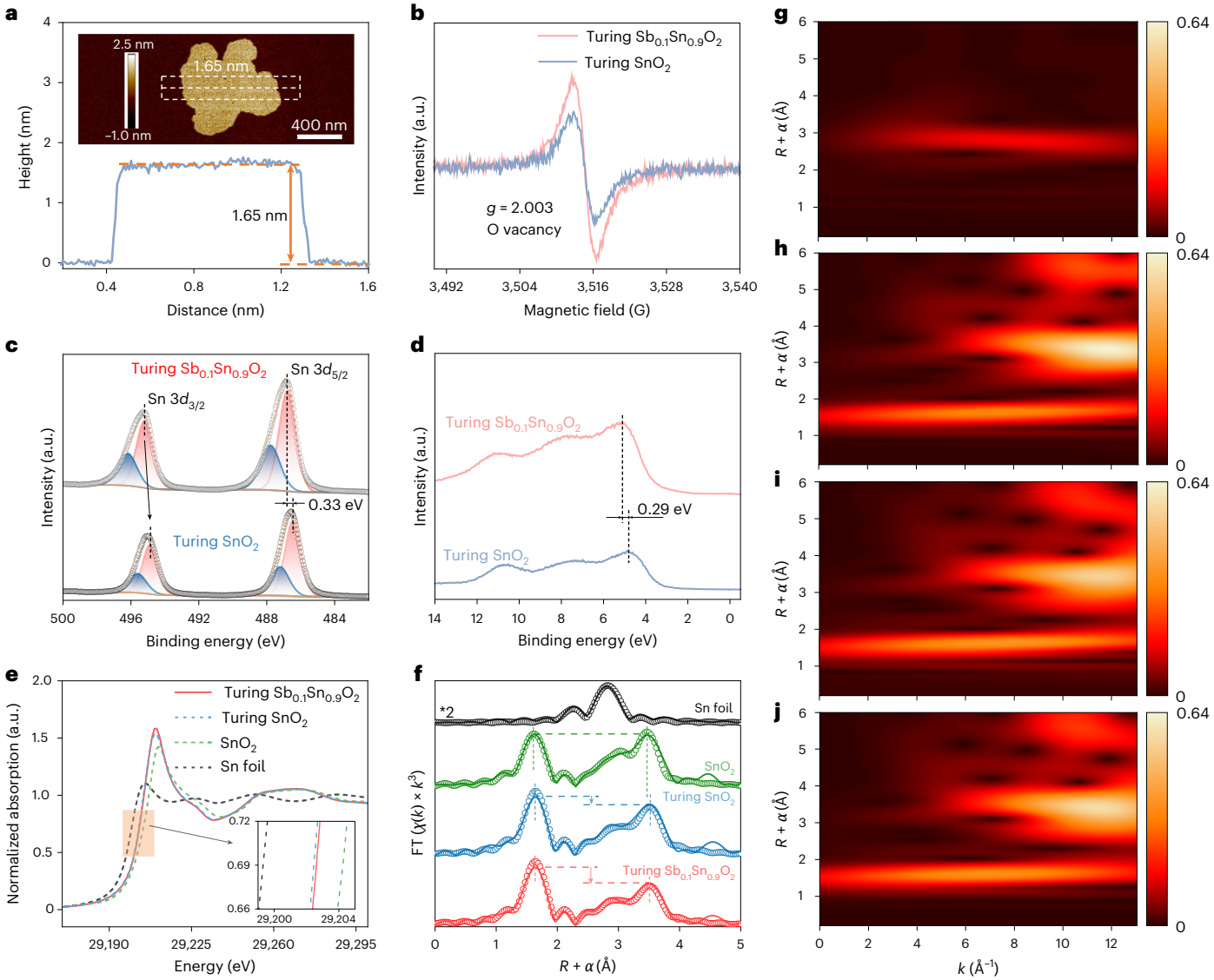

Fig. 2 | Fine-structure characterizations of Turing $Sb_{0.1}Sn_{0.9}O_2$. **a**, Atomic force microscopy image of Turing $Sb_{0.1}Sn_{0.9}O_2$. Inset: corresponding height profiles. **b**, Electron paramagnetic resonance signals. *g* represents intrinsic properties of unpaired electrons. **c**,**d**, High-resolution XPS spectra of the Sn 3*d* (**c**) and the valence band (**d**) of Turing $Sb_{0.1}Sn_{0.9}O_2$ and Turing SnO_2. **e**, Normalized Sn K-edge XANES spectra of Turing $Sb_{0.1}Sn_{0.9}O_2$, Turing SnO_2, SnO_2 and antimony foil. Inset: the corresponding magnified pre-edge XANES region. **f**, Fourier transform of Sn K-edge EXAFS spectra (circles) and corresponding fitting curves (solid line) in the R-space of Turing $Sb_{0.1}Sn_{0.9}O_2$, Turing SnO_2, SnO_2 and antimony foil. Data are k^3-weighted and not phase-corrected. *2 represents 2 times. **g**–**j**, Wavelet transform plots for the k^3-weighted Sn K-edge EXAFS of antimony foil (**g**), SnO_2 (**h**), Turing SnO_2 (**i**) and Turing $Sb_{0.1}Sn_{0.9}O_2$ (**j**).

with Turing SnO_2 (51.5 cm^2 cm^{-2}) and commercial SnO_2 (22.3 cm^2 cm^{-2}), illustrating that Turing $Sb_{0.1}Sn_{0.9}O_2$ possesses greater numbers of effective active sites. Taken together, these results demonstrate that Turing $Sb_{0.1}Sn_{0.9}O_2$ is an effective catalyst to enhance CO_2RR activity and selectivity at ampere-level current densities. We have further quantified the performance of Turing $Sb_{0.1}Sn_{0.9}O_2$ and Turing SnO_2 in acidic flow cells at the ampere level (pH 3, 0.5 M K_2SO_4 + H_2SO_4 solution, Supplementary Fig. 20). Turing $Sb_{0.1}Sn_{0.9}O_2$ presents a $FE_{formate}$ of 91.3% at 1,000 mA cm^{-2}, higher than that of Turing SnO_2 (58.4%), implying that Turing $Sb_{0.1}Sn_{0.9}O_2$ can operate in acidic medium at high industrial-level current density.

To further validate the potential of Turing $Sb_{0.1}Sn_{0.9}O_2$ in practical applications, the electrochemical activity and stability of Turing $Sb_{0.1}Sn_{0.9}O_2$ were investigated with a zero-gap MEA electrolyser (5 cm^2) at high current densities (Supplementary Figs. 21 and 22). As revealed in Fig. 3d, at an industrially relevant current density of 500 mA cm^{-2} (2,500 mA), Turing $Sb_{0.1}Sn_{0.9}O_2$ delivers outstanding stability of 200 h with an average $FE_{formate}$ of 82% at ~3.3 V in the MEA cell, contributing to the outstanding full-cell energy efficiency of 39.1% and formation rate of formate of 8.0 mmol h^{-1} cm^{-2}. Additionally, XRD patterns, HRTEM images and EDS mapping results (Supplementary Figs. 23–27) reveal that the Turing structure of Turing $Sb_{0.1}Sn_{0.9}O_2$ was retained without obvious aggregation after the stability tests, indicating that Turing structure-derived evolution may also be advantageous for CO_2-to-formate conversion. Furthermore, the single pass carbon efficiency (SPCE) of CO_2 for formate production and the full-cell energy efficiency in the MEA electrolyser for achieving industrial-level CO_2 electroreduction to formate reach 73.3% and 51.1% respectively, much higher than previously reported values[31–34], further endorsing the superiority of Turing $Sb_{0.1}Sn_{0.9}O_2$ in terms of economics for industrial CO_2-to-formate conversions (Supplementary Fig. 28). Impressively, the excellent comprehensive electrochemical performances of Turing $Sb_{0.1}Sn_{0.9}O_2$ outperform reported state-of-the-art electrocatalysts for CO_2 reduction

https://doi.org/10.1038/s44160-025-00769-9

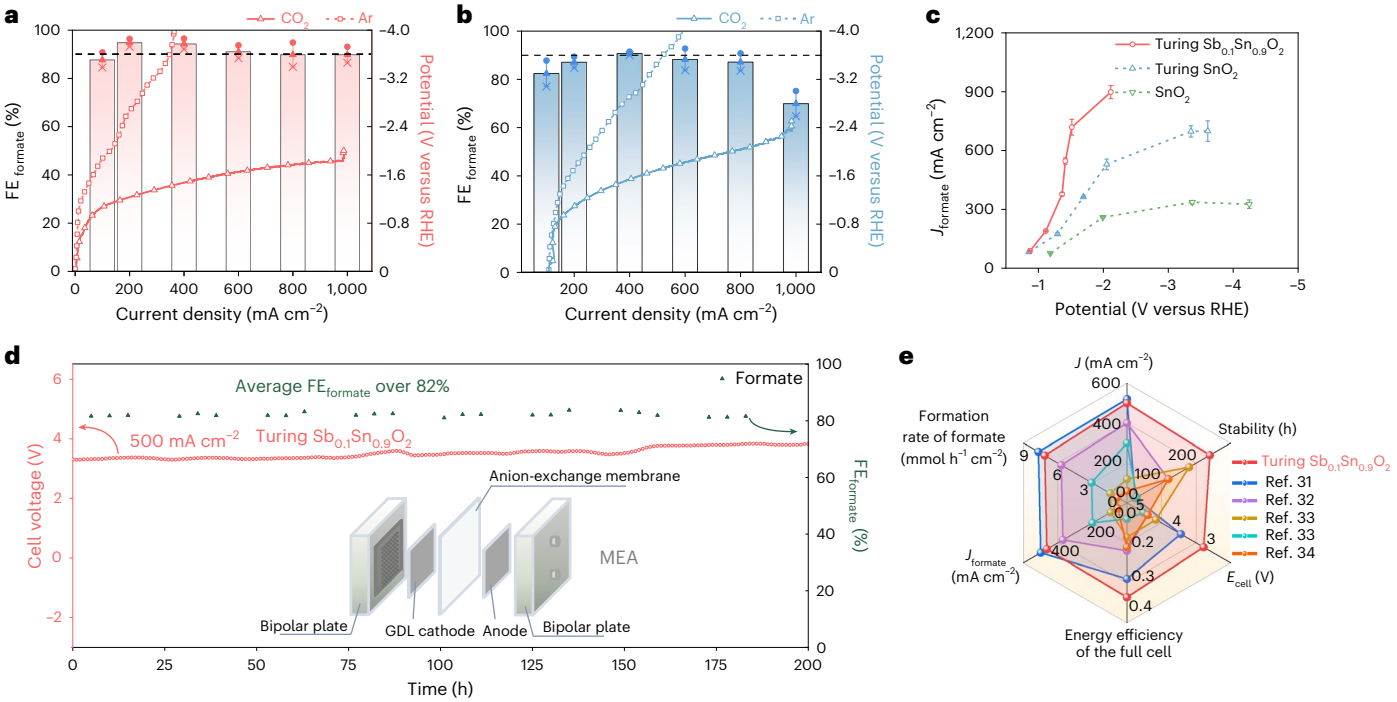

Fig. 3 | CO_2RR performance of Turing $Sb_{0.1}Sn_{0.9}O_2$ in flow cells and a MEA electrolyser at the ampere level. a,**b**, LSV curves of Turing $Sb_{0.1}Sn_{0.9}O_2$ (**a**) and Turing SnO_2 (**b**), and $FE_{formate}$ over Turing $Sb_{0.1}Sn_{0.9}O_2$ (**a**) and Turing SnO_2 (**b**) at different current densities under argon and CO_2 atmospheres. Data were recorded using flow cells with 0.5 M $KHCO_3$. The error bars represent the s.d. ($n = 3$ replicates); data are presented as mean ± s.d. **c**, $J_{formate}$ of the Turing $Sb_{0.1}Sn_{0.9}O_2$, Turing SnO_2 and SnO_2 catalysts as a function of the recorded potentials in 0.5 M $KHCO_3$. The error bars represent the s.d. ($n = 3$ replicates); data are presented as mean ± s.d. **d**, Durability test (red line) and corresponding $FE_{formate}$ (green dots) of continuous 200 h electrolysis in a 5-cm^2 MEA electrolyser under a constant total current density of 500 mA cm^{-2}. Inset: schematic illustration of the MEA configuration. **e**, Performance comparison of E_{cell}, stability, formation rate, total current density, $J_{formate}$ and full-cell energy efficiency with recently reported state-of-the-art CO_2RR-to-formate catalysts in MEA electrolysers.

to formate in MEA electrolysers (Fig. 3e)[31–34], enabling it to be a potential candidate catalyst for industrial-level CO_2RR-to-formate conversion.

Reaction microenvironment modulation on Turing $Sb_{0.1}Sn_{0.9}O_2$

Electrochemical reactions typically occur at the electrified electrode–electrolyte interface, also known as the interfacial microenvironment, greatly affecting the electrochemical performance especially at high current densities. To gain molecule-level insight into the microenvironment at the Turing $Sb_{0.1}Sn_{0.9}O_2$ electrode–electrolyte interface during the CO_2RR process, in situ attenuated total reflection surface-enhanced infrared absorption spectroscopy (ATR-SEIRAS) measurements were performed (Fig. 4). The coverage of the peak at ~1,400 cm^{-1} (Fig. 4a–c) associated with *OCHO intermediates over Turing $Sb_{0.1}Sn_{0.9}O_2$ at relatively high overpotentials (−0.9 V) is close to that of Turing SnO_2 and much higher than that of SnO_2, indicating higher local accumulation of *OCHO on Turing configurations, consistent with the activity trend of the three catalysts at high current densities (Fig. 3a–c). Similarly, the coverage of the peak at ~3,600 cm^{-1} on Turing-type catalysts associated with stretching of OH[19,21,35] is much higher at relatively high overpotentials (−0.9 V) than that of SnO_2 (Fig. 4a–c), further implying high oxophilicity of Turing structures and thus affecting the formation of the oxygen-associated intermediates[10].

Note that the OH stretching vibration is also closely associated with the interfacial water, which further considerably affects the interfacial water microenvironment and proton transfer, thus possibly affecting the CO_2RR performance at high current densities[3,20,21,36]. To qualitatively assess the interfacial water microenvironment effect on CO_2RR at high current densities, the peaks of interfacial water bands at around 3,600 cm^{-1} are resolved into three components, that is, the peaks at 3,600 cm^{-1}, 3,450 cm^{-1} and 3,270 cm^{-1}, assigned to free water, two-coordinated hydrogen-bonded water (weakly hydrogen-bonded, 2-HB water) and four-coordinated hydrogen-bonded water (strongly hydrogen-bonded, 4-HB water)[20,36], respectively (Fig. 4d–f). The proportions of quantitatively normalized peak areas are shown in Fig. 4g–i. As observed in Fig. 4d–f, the variation in the OH stretching vibration frequencies from 3,400 cm^{-1} to 3,270 cm^{-1} indicates altered interfacial water components, corresponding to the SnO_2, Turing $Sb_{0.1}Sn_{0.9}O_2$ and Turing SnO_2 catalysts.

The larger 4-HB/2-HB interfacial water ratios on Turing structures (3.10 for Turing SnO_2, 1.60 for Turing $Sb_{0.1}Sn_{0.9}O_2$) compared with that of non-Turing structures (0.26 for SnO_2) imply strengthened hydrogen-bond networks[3,20] at the electrode–electrolyte interface of Turing structures. It also suggests that the orientation of interfacial water is greatly affected by the nature of Turing structures. Impressively, the trend of the 4-HB/2-HB ratio is consistent with the catalytic performance trend based on the LSV curves under argon for these catalysts (Fig. 3a,b and Supplementary Figs. 16 and 17), which is associated with the competing HER, implying that the large 4-HB/2-HB ratio potentially accelerates the HER. This evidence demonstrates that Turing structures are favourable for tuning the oxophilicity of catalysts, which affects the formation of the *OCHO intermediates and induces variation in the orientation of hydrogen-bond networks, thus modulating catalysts and the interfacial water microenvironment at the electrode–electrolyte interface.

Mechanistic mechanism

To further uncover the underlying mechanism for the roles of Turing structures and oxophilicity in promoting CO_2RR-to-formate processes, density functional theory calculations were carried out (Supplementary Figs. 29–32). Figure 5a shows that there is an obvious separation of the

https://doi.org/10.1038/s44160-025-00769-9

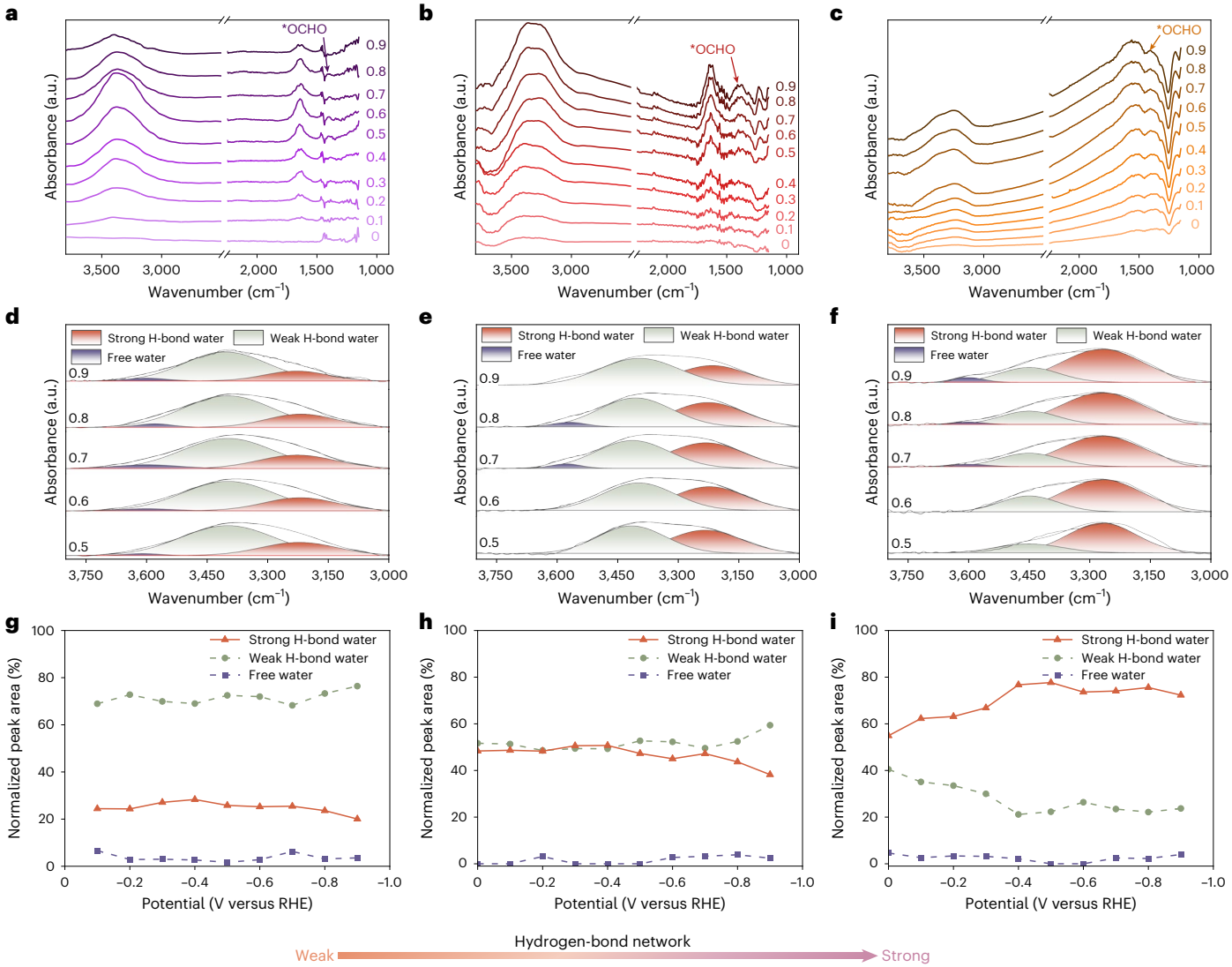

Fig. 4 | In situ spectroscopic evidence for microenvironment modulation. **a**–**c**, In situ ATR-SEIRAS spectra measured at various potentials on SnO_2 (**a**), Turing $Sb_{0.1}Sn_{0.9}O_2$ (**b**) and Turing SnO_2 (**c**) in 0.5 M $KHCO_3$. **d**–**f**, Potential-dependent fitted bands of interfacial water at 3,750–3,000 cm^{-1} on SnO_2 (**d**), Turing $Sb_{0.1}Sn_{0.9}O_2$ (**e**) and Turing SnO_2 (**f**). **g**–**i**, Variation in the proportion of interfacial water on SnO_2 (**g**), Turing $Sb_{0.1}Sn_{0.9}O_2$ (**h**) and Turing SnO_2 (**i**) versus various potentials.

electronic orbitals for Turing-type catalysts relative to non-Turing-type catalysts. Figure 5b and Supplementary Figs. 33 and 34 show the corresponding free-energy diagrams of the CO_2RR to formate on these catalysts. In comparison with that of non-Turing SnO_2, the lower energy of *OCHO intermediate formation at various applied potentials for Turing SnO_2 and Turing $Sb_{0.1}Sn_{0.9}O_2$ implies that Turing configuration contributes to the formation of *OCHO intermediates, which are vital intermediates for CO_2RR-to-formate conversions, thereby benefiting the formation of formate, in line with the in situ ATR-SEIRAS and electrocatalytic results.

Importantly, there is also an observed increase in *OCHO adsorption energy in the order $Sb_{0.1}Sn_{0.9}O_2$ (0.09 eV) < SnO_2 (−0.02 eV) < Turing $Sb_{0.1}Sn_{0.9}O_2$ (−0.43 eV) < Turing SnO_2 (−0.62 eV) (Fig. 5c), in line with the sequence of the p-band centre ($Sb_{0.1}Sn_{0.9}O_2$ (−3.82 eV) < SnO_2 (−3.26 eV) < Turing $Sb_{0.1}Sn_{0.9}O_2$ (−0.79 eV) < Turing SnO_2 (−0.71 eV) (Supplementary Fig. 35), indicating the sequence of enhanced oxophilicity. These results indicate that doping antimony into SnO_2 leads to a slight decrease in oxophilicity. Conversely, this evidence also indicates that Turing structures are favourable for enhancing the oxophilicity, in agreement with the experimental observations of the distance and coordination number by EXAFS, the coverage of OH and *OCHO by in situ ATR Fourier transform infrared (FTIR) spectroscopy and XPS, and the corresponding valence band results, and with the crystal orbital Hamilton population (Supplementary Fig. 36) and the Bader charge results (Supplementary Table 2). Our findings indicate that the adsorption energy of the *OCHO intermediates is enhanced on the interface of Turing configurations (SnO_2, −0.02 eV; Turing $Sb_{0.1}Sn_{0.9}O_2$, −0.43 eV; Turing SnO_2, −0.62 eV), indicating that the interface of the Turing configurations is favourable for the adsorption of the key intermediates for CO_2RR-to-formate conversions, in agreement with the in situ ATR-FTIR and electrocatalytic results. These results confirm that the construction of Turing-type catalysts with dopants serves as an effective method for tuning oxophilicity, in which Turing configurations account for the considerably enhanced oxophilicity.

Taking the sequence of oxophilicity we have determined here in combination with the above in situ ATR-FTIR results (Fig. 4) and electrochemical performance (Fig. 3 and Supplementary Figs. 16 and 17) reveals that, under high current densities, increasing oxophilicity induces the enhancement of hydrogen-bond networks with large 4-HB/2-HB interfacial water ratios accompanied by an increase in the

https://doi.org/10.1038/s44160-025-00769-9

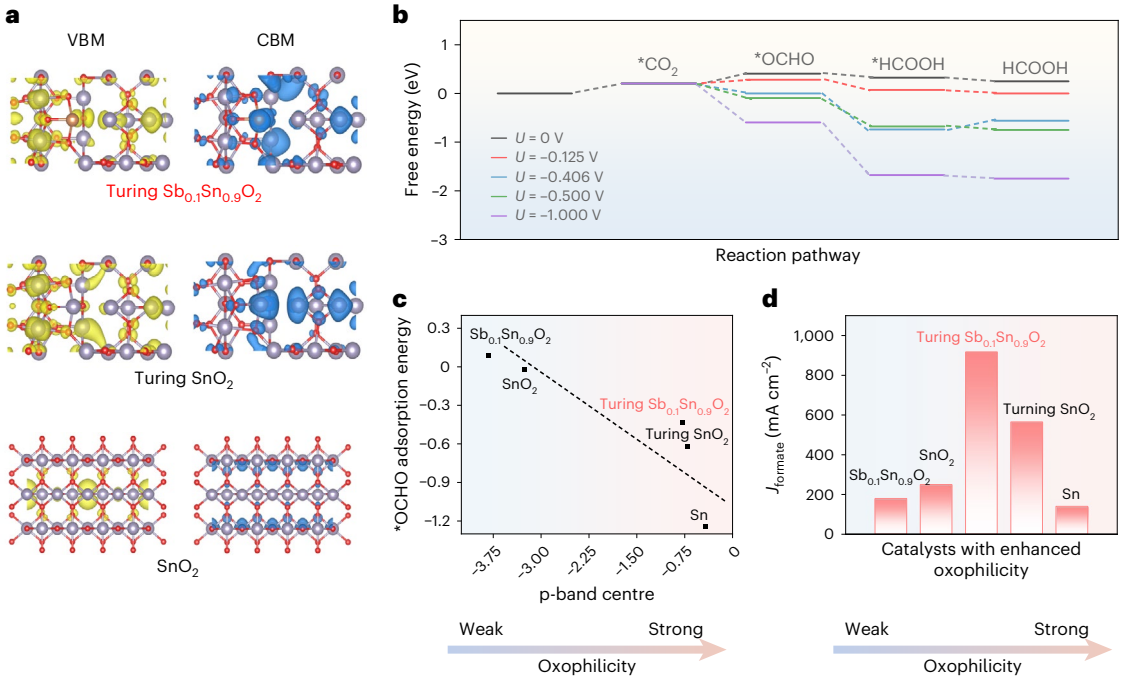

Fig. 5 | Correlations between theoretical descriptors and properties. **a**, Electronic orbitals of the valence band maximum (VBM) and the conduction band minimum (CBM) of Turing $Sb_{0.1}Sn_{0.9}O_2$, Turing SnO_2 and SnO_2. **b**, Free-energy diagrams of the CO_2RR to formate on Turing $Sb_{0.1}Sn_{0.9}O_2$ at different applied potentials. *U* means the applied potential. **c**, The p-band-centre-dependent adsorption energy of the *OCHO intermediates on Turing $Sb_{0.1}Sn_{0.9}O_2$, Turing SnO_2, $Sb_{0.1}Sn_{0.9}O_2$, SnO_2 and antimony. **d**, A volcano-like relationship between oxophilicity and partial current densities of formate at −1.6 V versus RHE on these catalysts.

competing HER. Conversely, decreasing oxophilicity induces weakened *OCHO adsorption accompanied by inhibited CO_2RR kinetics. This can be further verified in Fig. 5d, where the high current densities show a volcano-shaped dependence on the oxophilicity of these catalysts. Turing $Sb_{0.1}Sn_{0.9}O_2$ with optimal oxophilicity reaches the summit of the volcano, which stands out for having excellent ampere-level current densities and durability due to the balance of hydrogen transfer from the reaction microenvironment by tuning the 4-HB/2-HB interfacial water ratios at the electrode–electrolyte interface.

Conclusions

We construct a series of Turing-structured topology catalysts and precisely modulate the reorientation of 4-HB/2-HB interfacial water (with ratios ranging from 0.26 to 3.10) by tuning their surface oxophilicity to achieve industrial-level CO_2-to-formate electrolysis. Based on the manipulated interfacial hydrogen-bond networks, we demonstrate the oxophilicity of the Turing-structured catalysts as a viable descriptor to track the efficiency of CO_2-to-formate conversion over a range of industrially relevant current densities (300–1,000 mA cm^{-2}). The current densities and oxophilicities display a volcano relation: weak oxophilicity induces low adsorption of *OCHO intermediates due to the slow hydrogenation of CO_2RR, whereas strong oxophilicity leads to the competing HER due to the strengthened hydrogen-bond networks. The optimal Turing $Sb_{0.1}Sn_{0.9}O_2$ catalyst, with 4-HB/2-HB interfacial water ratios of 1, reaches a $FE_{formate}$ of 92% at 1,000 mA cm^{-2} in a flow cell and delivers a stability of 200 h with an average $FE_{formate}$ of 82% at ~3.3 V in a MEA electrolyser under 500 mA cm^{-2}, contributing to the excellent full-cell energy efficiency of 39.1% and a formate formation rate of of 8.0 mmol h^{-1} cm^{-2}.

Methods

Synthesis of Turing $Sb_{0.1}Sn_{0.9}O_2$

For a typical synthesis of Turing $Sb_{0.1}Sn_{0.9}O_2$, 3.76 g of glycine and 3.66 ml of concentrated HCl were added to ethylene glycol (450 ml) with ultrapure water (50 ml) and ultrasonically dispersed to form a buffer solution, followed by the addition of rGO (50 mg) and $SnCl_4$ (5 mmol). The mixture was heated to 70 °C for 24 h with magnetic agitation. Subsequently, the resulting suspension was washed by centrifugation with ultrapure water, and was then freeze-dried for 48 h. Finally, Turing $Sb_{0.1}Sn_{0.9}O_2$ was obtained by calcining the obtained powder in air at 650 °C for 2 h to remove the rGO template.

In situ ATR-SEIRAS measurements

In situ ATR-SEIRAS spectra were obtained on an FTIR spectrometer (Bruker 70V). An Ag/AgCl electrode and a platinum wire were used as the reference and counter-electrodes, respectively. The working electrode was prepared by dropping a homogeneous catalyst ink onto a gold-coated hemispherical silicon prism. Before in situ ATR-SEIRAS measurements, 0.5 M $KHCO_3$ electrolyte needed to be saturated with CO_2. Then, in situ ATR-SEIRAS spectra were collected at a potential range of 0 to −0.9 V versus RHE (reversible hydrogen electrode) using OMNIC software in series mode. Each spectrum was acquired at a resolution of 8 cm^{-1}.

Electrochemical measurements

All the electrochemical measurements of the CO_2RR were carried out in a CHI 660E electrochemical workstation. CO_2RR activity measurements at large current densities were performed in 0.5 M $KHCO_3$ electrolytes by using a flow cell with a three-electrode system, in which Ag/AgCl served as the reference electrode and IrO_x/Ti foam served as the counter-electrode. The working electrode consisted of a gas-diffusion layer (GDL, Sigracet 29BC) with a homogeneous catalyst ink air-brushed onto its surface. The catalyst ink was prepared by mixing 2 mg of catalyst, 10 µl of Nafion (Dupont, 5%) and 1 ml of an ultrapure water/isopropanol (1:1) solution, and was further ultrasonicated for 1 h. An anion-exchange membrane (Sustainion X37-50 RT) was located between the cathode and anode to separate the chambers. The applied potentials were calibrated to RHE via the equation (*E* (versus RHE) =

E (versus Ag/AgCl) + 0.197 V + 0.059 pH). Manual iR correction of 85% in the three-electrode system was conducted during the measurements. The solution resistance was determined by electrochemical impedance spectroscopy measurements in the frequency range 0.1 Hz–100 kHz. Gaseous products were evaluated by using an online gas chromatograph (Agilent). Liquid products were quantitatively detected by NMR measurements.

CO_2RR durability measurements at high current densities were obtained in a commercial 5-cm^2 MEA electrolyser (Dioxide Materials) with a two-electrode system, in which IrO_x/Ti foam served as the anode. The catalysts (1.5 mg cm^{-2}), VXC-72 Cabot black carbon (0.2 mg cm^{-2}) and Nafion (5%) were ultrasonically mixed and then air-brushed on a GDL (Sigracet 29BC), which served as the cathode. An anion-exchange membrane (Sustainion X37-50 RT) was located between the cathode and anode to separate the chambers. The full-cell potentials in the two-electrode MEA system are shown without iR correction. During the CO_2RR in the MEA electrolyser, the anode electrolyte (0.02 M Cs_2CO_3) was flowed through the anode at a flow rate of 10 ml min^{-1}, while high-purity CO_2 was flowed over the back of the GDL at the cathode at a flow rate of 35 sccm by an electronic flowmeter. The electrochemically active surface area can be determined at the base of the double-layer capacitor by using cyclic voltammetry at various scan rates in the non-Faradaic potential regions[22,37]. More details are provided in the Supplementary Information.

Data availability

The data supporting the findings of this study are available within the Article and its Supplementary Information files.

References

1. Gomes, R. J. et al. Modulating water hydrogen bonding within a non-aqueous environment controls its reactivity in electrochemical transformations. *Nat. Catal.* **7**, 689–701 (2024).
2. Chu, A. T. et al. Organic non-nucleophilic electrolyte resists carbonation during selective CO_2 electroreduction. *J. Am. Chem. Soc.* **145**, 9617–9623 (2023).
3. Zhang, H. et al. Promoting Cu-catalysed CO_2 electroreduction to multicarbon products by tuning the activity of H_2O. *Nat. Catal.* **6**, 807–817 (2023).
4. Fang, W. et al. Durable CO_2 conversion in the proton-exchange membrane system. *Nature* **626**, 86–91 (2024).
5. Fernández-Caso, K. et al. Electroreduction of CO_2: advances in the continuous production of formic acid and formate. *ACS Energy Lett.* **8**, 1992–2024 (2023).
6. Yu, X. et al. Coverage enhancement accelerates acidic CO_2 electrolysis at ampere-level current with high energy and carbon efficiencies. *Nat. Commun.* **15**, 1711 (2024).
7. Ren, B. et al. Nano-crumples induced Sn–Bi bimetallic interface pattern with moderate electron bank for highly efficient CO_2 electroreduction. *Nat. Commun.* **13**, 2486 (2022).
8. Peng, C. et al. Ampere-level CO_2-to-formate electrosynthesis using highly exposed bismuth(110) facets modified with sulfur-anchored sodium cations. *Chem* **9**, 2830–2840 (2023).
9. Ko, Y. J. et al. Exploring dopant effects in stannic oxide nanoparticles for CO_2 electro-reduction to formate. *Nat. Commun.* **13**, 2205 (2022).
10. Zhang, L. et al. Oxophilicity-controlled CO_2 electroreduction to C_{2+} alcohols over Lewis acid metal-doped $Cu^{\delta+}$ catalysts. *J. Am. Chem. Soc.* **145**, 21945–21954 (2023).
11. Li, Z. et al. Directing CO_2 electroreduction pathways for selective C_2 product formation using single-site doped copper catalysts. *Nat. Chem. Eng.* **1**, 159–169 (2024).
12. Zeng, M. et al. Reaction environment regulation for electrocatalytic CO_2 reduction in acids. *Angew. Chem. Int. Ed.* **63**, e202404574 (2024).
13. Wang, D. et al. Modulating microenvironments to enhance CO_2 electroreduction performance. *eScience* **3**, 100119 (2023).
14. Zhang, Z. et al. Probing electrolyte effects on cation-enhanced CO_2 reduction on copper in acidic media. *Nat. Catal.* **7**, 807–817 (2024).
15. Ma, X. et al. Hydrogen-bond network promotes water splitting on the TiO_2 surface. *J. Am. Chem. Soc.* **144**, 13565–13573 (2022).
16. Ge, W. et al. Dynamically formed surfactant assembly at the electrified electrode–electrolyte interface boosting CO_2 electroreduction. *J. Am. Chem. Soc.* **144**, 6613–6622 (2022).
17. Wang, Y. et al. Strong hydrogen-bonded interfacial water inhibiting hydrogen evolution kinetics to promote electrochemical CO_2 reduction to C_{2+}. *ACS Catal.* **14**, 3457–3465 (2024).
18. Chen, X. et al. Promoting water dissociation for efficient solar driven CO_2 electroreduction via improving hydroxyl adsorption. *Nat. Commun.* **14**, 751 (2023).
19. Fan, Y. et al. Mechanistic insights into surfactant-modulated electrode–electrolyte interface for steering H_2O_2 electrosynthesis. *J. Am. Chem. Soc.* **146**, 7575–7583 (2024).
20. Wang, Y. H. et al. In situ Raman spectroscopy reveals the structure and dissociation of interfacial water. *Nature* **600**, 81–85 (2021).
21. Li, P. et al. Hydrogen bond network connectivity in the electric double layer dominates the kinetic pH effect in hydrogen electrocatalysis on Pt. *Nat. Catal.* **5**, 900–911 (2022).
22. Sun, Q. et al. Understanding hydrogen electrocatalysis by probing the hydrogen-bond network of water at the electrified Pt–solution interface. *Nat. Energy* **8**, 859–869 (2023).
23. Ma, Z. et al. CO_2 electroreduction to multicarbon products in strongly acidic electrolyte via synergistically modulating the local microenvironment. *Nat. Commun.* **13**, 7596 (2022).
24. Gu, J. et al. Turing structuring with multiple nanotwins to engineer efficient and stable catalysts for hydrogen evolution reaction. *Nat. Commun.* **14**, 5389 (2023).
25. Gu, J. et al. Twinning engineering of platinum/iridium nanonets as Turing-type catalysts for efficient water splitting. *J. Am. Chem. Soc.* **146**, 5355–5365 (2024).
26. Tan, Z. et al. Polyamide membranes with nanoscale Turing structures for water purification. *Science* **360**, 518–521 (2018).
27. Zhang, X. L. et al. An efficient Turing-type Ag_2Se–$CoSe_2$ multi-interfacial oxygen-evolving electrocatalyst. *Angew. Chem. Int. Ed.* **60**, 6553–6560 (2021).
28. Li, X. Y. et al. Constrained minimal-interface structures in polycrystalline copper with extremely fine grains. *Science* **370**, 831–836 (2020).
29. Hu, C. et al. Misoriented high-entropy iridium ruthenium oxide for acidic water splitting. *Sci. Adv.* **9**, f9144 (2023).
30. Zhang, Y. et al. Homogeneous solution assembled Turing structures with near zero strain semi-coherence interface. *Nat. Commun.* **13**, 2942 (2022).
31. Bi, J. et al. High-rate CO_2 electrolysis to formic acid over a wide potential window: an electrocatalyst comprised of indium nanoparticles on chitosan-derived graphene. *Angew. Chem. Int. Ed.* **62**, e202307612 (2023).
32. Shen, H. et al. In-situ constructing of copper-doped bismuth catalyst for highly efficient CO_2 electrolysis to formate in ampere-level. *Adv. Energy Mater.* **13**, 2202818 (2023).
33. Li, L. et al. Stable, active CO_2 reduction to formate via redox-modulated stabilization of active sites. *Nat. Commun.* **12**, 5223 (2021).
34. Yan, S. et al. Electron localization and lattice strain induced by surface lithium doping enable ampere-level electrosynthesis of formate from CO_2. *Angew. Chem. Int. Ed.* **60**, 25741–25745 (2021).
35. Chen, X. et al. Revealing the role of interfacial water and key intermediates at ruthenium surfaces in the alkaline hydrogen evolution reaction. *Nat. Commun.* **14**, 5289 (2023).

36. Liu, Z. et al. Interfacial water tuning by intermolecular spacing for stable CO_2 electroreduction to C_{2+} products. *Angew. Chem. Int. Ed.* **62**, e202309319 (2023).
37. Ye, F. et al. The role of oxygen-vacancy in bifunctional indium oxyhydroxide catalysts for electrochemical coupling of biomass valorization with CO_2 conversion. *Nat. Commun.* **14**, 2040 (2023).

Acknowledgements

This work was financially supported by the Science and Technology Innovation Project of Laoshan Laboratory (LSKJ202205400), the National Science Fund for Distinguished Young Scholars (number 52025133), the Beijing Outstanding Young Scientist Program (JWZQ20240102004), the National Science Fund for Young Scholars (numbers 22102003, 22409009), the China National Petroleum Corporation-Peking University Strategic Cooperation Project of Fundamental Research, the Beijing Natural Science Foundation (number Z220020), the Tencent Foundation through the XPLORER PRIZE, the CNPC Innovation Fund (2021DQ02-1002) and the China Postdoctoral Science Foundation (grant number 2023M730052).

Author contributions

S.G. conceived the project. N.Y. and M.L. designed the research, and performed the material synthesis, characterization and electrochemical tests. K.W., Y.T., Z.Q., Z.L. and Q.H. participated in assembling and testing the MEA. N.Y. and Y.L. carried out the XAFS data analysis. H.G., C.S., Y.H. and C.Z. performed the HAADF-STEM characterization. L.L. and Y.G. conducted the density functional theory calculations. S.G. and N.Y. wrote the paper. All authors participated in the project discussions and production of the final manuscript.

Competing interests

The authors declare no competing interests.

Additional information

Supplementary information The online version contains supplementary material available at https://doi.org/10.1038/s44160-025-00769-9.

Correspondence and requests for materials should be addressed to Shaojun Guo.

Peer review information *Nature Synthesis* thanks the anonymous reviewers for their contribution to the peer review of this work. Primary Handling Editor: Alexandra Groves, in collaboration with the *Nature Synthesis* team.